



Identification of Desirable Precursor Properties for Solution Precursor Plasma Spray

Chigozie K. Muoto, Eric H. Jordan, Maurice Gell, and Mark Aindow

(Submitted December 20, 2010; in revised form February 21, 2011)

In solution precursor plasma spray chemical precursor solutions are injected into a standard plasma torch and the final material is formed and deposited in a single step. This process has several attractive features, including the ability to rapidly explore new compositions and to form amorphous and metastable phases from molecularly mixed precursors. Challenges include: (a) moderate deposition rates due to the need to evaporate the precursor solvent, (b) dealing on a case by case basis with precursor characteristics that influence the spray process (viscosity, endothermic and exothermic reactions, the sequence of physical states through which the precursor passes before attaining the final state, etc.). Desirable precursor properties were identified by comparing an effective precursor for yttria-stabilized zirconia with four less effective candidate precursors for $\text{MgO}:\text{Y}_2\text{O}_3$. The critical parameters identified were a lack of major endothermic events during precursor decomposition and highly dense resultant particles.

Keywords influence of spray parameters, nanocrystalline composites, reactive spraying, solution precursor PS

1. Introduction

Plasma spraying is a well-established method for depositing functional coatings on structural components to provide resistance to heat, wear, corrosion, etc. (Ref 1, 2). For example, this technology has been applied extensively in the deposition of thermal barrier coatings (TBCs) on internally cooled, hot-section components in gas turbine engines for the thermal protection of the base metals, affording higher, and therefore more efficient, operating temperatures (Ref 3). Various different plasma-spraying techniques have been developed. These include: the conventional air plasma spray (APS), suspension plasma spray (SPS), and solution precursor plasma spray (SPPS) processes (Ref 4-6). These are categorized based on the feedstock material injected into the plasma jet during the spraying process.

In the APS process, solid powder particles in the size range of 30-70 μm are injected into the plasma jet, where they are melted and propelled onto the prepared substrate to produce lamellar structures. It is generally not possible

to feed particles finer than 5-10 μm due to the insufficient momentum of the particles for entrainment in the plasma jet (Ref 7, 8).

The SPS process was developed, in part to overcome the particle entrainment issue associated with the injection of such fine powders into the plasma jet. In the SPS process, submicron or nanosized particles are suspended in a liquid and the suspension is injected into the plasma jet, where a rapid vaporization of the liquid occurs to expose the particles to the plasma heat. The fine particles, which otherwise would not be entrained in the plasma jet, are melted and deposited on the substrate as thin “splats.” Nanopowders in suspension have the potential to produce nanostructured ceramic coatings, which leads to improvements in certain desirable mechanical properties such as strength and hardness (Ref 9).

The SPPS process also deposits melted feedstock material onto a substrate as splats, which are layered to form a lamellar-structured coating. However, the primary differentiating attribute between SPPS and other deposition methods is that the feedstock material is in the form of a liquid solution, rather than a powder or a suspension. As a result, the SPPS process can potentially deliver deposits with finer microstructures in a single step, combining synthesis and consolidation processes of nanograins in one operation, without the difficulties and limitations of both fabricating and feeding solid powders.

The most highly explored area for the SPPS technology has been in the deposition of zirconia-based material systems, such as yttria-stabilized zirconia (YSZ), for application as TBCs (Ref 10-13). SPPS TBCs have some unique and desirable microstructural characteristics not found in TBCs deposited using other processes. These include: (1) through-thickness vertical cracks, (ii) lack of

Chigozie K. Muoto, Maurice Gell, and Mark Aindow, Department of Chemical, Materials and Biomolecular Engineering, Institute of Materials Science, University of Connecticut, Storrs, CT 06269; and **Eric H. Jordan**, Department of Mechanical Engineering, Institute of Materials Science, University of Connecticut, Storrs, CT 06269. Contact e-mail: jordan@enr.uconn.edu.



the deleterious large-scale “splat” boundaries, which are found in TBCs deposited using the APS technique, and (iii) controlled porosity. As a result, TBCs produced by SPPS offer the potential of increased durability and lower thermal conductivity compared to those produced using other techniques (Ref 14-19).

The SPPS process also has other attractive attributes that could make it amenable to a wide variety of applications. Multicomponent materials can be generated quickly using this process, circumventing the laborious powder synthesis and mixing processes. Moreover, the ease of formulating new solution compositions by mixing of precursors in the appropriate proportions offers a quick and precise method for controlling the chemistry of the deposit and the ability to deposit compositionally graded coatings with ease. Since the process uses precursor solutions that are molecularly mixed, good chemical homogeneity of the deposit is easily achieved (Ref 4). For example, the SPPS process has been applied successfully to the deposition of Ni-YSZ anodes for solid oxide fuel cells (SOFCs), where a homogenous distribution of YSZ particles in a continuous Ni matrix was obtained (Ref 20). In addition, the SPPS process is capable of creating metastable phases in the deposits due to rapid cooling of the ultra-fine splats during deposition (Ref 21, 22).

There are, however, drawbacks and challenges in using the SPPS process, particularly in the fabrication of dense ceramic coatings where a good percentage of the particles arriving at the substrate during the spraying process are required to be in the molten state. A precursor droplet injected in the plasma jet must undergo a sequence of physical states before attaining the final molten state that leads to splat formation on the substrate. These include: precursor solvent evaporation, droplet break-up, precursor solute precipitation, gelation, pyrolysis (to form oxide particles), sintering, and melting of the particles (Ref 23). The densities of the coatings deposited, as well as the deposition efficiencies, are determined by the degree of completeness of the above series of reactions. The ability to fabricate dense coatings is greatly influenced by precursor characteristics, such as the solution molarity, the endo- or exothermicity of the thermal decomposition mechanisms for the constituent precursor chemicals, and the form of the reaction by-products. The latter issue is particularly important if the reaction by-products are porous due, for example, to gas released during the thermal decomposition reaction. If the reactions are incomplete, unmelted oxide particles and/or unpyrolyzed precursor droplets are deposited onto the substrate, which results in a porous, friable coating, and low deposition efficiency.

In our work, we have been investigating the use of SPPS to deposit dense Y_2O_3 -MgO nanocomposite pre-forms for the fabrication of optical windows. Several precursor types for this material system were explored in an effort to identify the key precursor properties for the deposition of dense Y_2O_3 -MgO nanocomposites. Our approach to understanding the phenomena involved was to compare the characteristics of zirconium acetate-based precursor solutions, which have been developed to yield

dense YSZ coatings, with candidate precursor solutions for the deposition of dense Y_2O_3 -MgO nanocomposite coatings. Our findings are presented in this article and the relationships between the precursor properties and coating morphologies are discussed. It is suggested that the precursor characteristics required for obtaining dense deposits can be generalized to other oxide materials. The goal is to move away from assessing precursors by making coatings and toward a faster assessment approach using simple lab tests and material properties or known reaction paths for the precursors.

2. Experimental Procedure

2.1 Solution Precursor Preparation

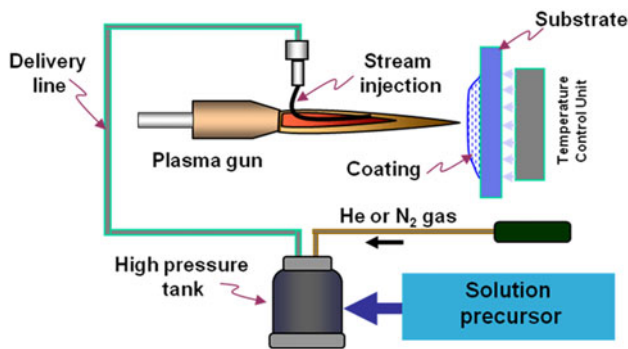
Four different types of precursor solution were explored for the plasma spray deposition of Y_2O_3 -MgO nanocomposites. These include: binary mixtures of yttrium nitrate (Y[n]) or yttrium acetate (Y[a]), combined with magnesium nitrate (Mg[n]) or magnesium acetate (Mg[a]), and using water as the solvent. The Y[n], Y[a], Mg[n], and Mg[a] salts used were: yttrium(III) nitrate hexahydrate ($Y(NO_3)_3 \cdot 6H_2O$, 99.9%), yttrium(III) acetate tetrahydrate ($Y(CH_3COO)_3 \cdot 4H_2O$, 99.9%), magnesium nitrate hexahydrate ($Mg(NO_3)_2 \cdot 6H_2O$, 98-102%) and magnesium acetate tetrahydrate ($Mg(CH_3COO)_2 \cdot 4H_2O$, 98-102%), respectively; all of these salts were purchased from Alfa Aesar (Ward Hill, MA). The proportions of the yttrium and magnesium salts in the solutions were selected such that the conversion of all of the cations to the corresponding oxides would give a 50-50 vol.% Y_2O_3 -MgO composite. We chose this composition because the interpenetrating phase mixture would be expected to have the greatest resistance to coarsening at elevated temperatures, with the grains of each phase pinning the boundaries in the other phase. The precursor solutions containing only nitrate salts were prepared at an ambient temperature of 25 °C, while those containing acetate salts were heated to and injected at a temperature of about 90 °C to increase solubility. Ammonium acetate (CH_3COONH_4 , 97.0%; Alfa Aesar), which is designated hereafter as $NH_4[a]$, was added to the Y[n]Mg[n] precursor solution to increase the exothermicity of the decomposition process. For the Y[n]Mg[n]+ $NH_4[a]$ mixture used here the quantity of $NH_4[a]$ was adjusted to 50% of that required for stoichiometric reaction. We note that acetates can oxidize in the air present during spraying, and that the nitrate can act as an oxidizer for the acetate in the acetate-nitrate combinations. For the 7 wt.% YSZ (7YSZ) deposition, Y[n] and a solution of zirconium acetate ($Zr(CH_3COO)_2$ -Zr[a]) in a liquid form (Inframat Advanced Materials, Manchester, CT) were used as the precursors.

2.2 Plasma Spray Deposition

The spray deposition experiments in this study were conducted using a direct current Metco 9 MB plasma gun (Sulzer Metco, Westbury, NY), which was attached to a

Table 1 Plasma spray parameters

Torch power, kW	Torch current, A	Exit nozzle, mm	Gas flowrate, scfh		Feedstock flowrate, L/min	Tank pressure, MPa	Spray distance, mm
			Ar	H ₂			
36-45.5	600-650	6-8	100-120	21-35	25-40	0.7-1.4	40-48
Torch transverse speed: 500 mm/s							

**Fig. 1** Schematic of the plasma spray process showing the setup for solution precursor plasma spray (SPPS) using stream injection

multi-axis robotic arm to allow for a programmable scanning of the plasma torch across a substrate. The primary and secondary gases were Ar and H₂, respectively. The current and voltage of the plasma arc, as well as the gas flow rates, were varied to give a plasma torch power ranging from 36 to 45.5 kW. The plasma spray parameters used are shown in Table 1.

Precursor delivery into the plasma jet was by means of stream injection using a high-pressure tank as shown in Fig. 1. For the injection (150 micron diameter) of heated precursor solutions, the tank and the delivery line were heated to about 90 and 150 °C, respectively. Three different sets of coating deposition experiments were performed in which deposits were collected on Type 304 stainless steel substrates (25.4 mm diameter and 3 mm thickness). In the first set of experiments, coatings were deposited by scanning the plasma torch across the substrate in a raster scan pattern as the feedstock was being injected into the plasma jet. Multiple scans were used to build-up the coatings. The second set of experiments also involved multiple scans, but in this case the plasma torch was programmed to scan across the substrate in a single line. Prior to the deposition process in these two sets of experiments, the substrate surface was roughened by grit blasting using Al₂O₃ #30 grit at ~60 psi. The substrates were also preheated to a temperature of ~300 °C, in order to enhance adherence of the coating to the substrate. However, there was an upward increment of substrate temperature during spraying. The highest temperature attained by the substrate was dependent on certain process variables such as spray distance, plasma torch power, primary and secondary gas flow rates, scan rates/steps, and number of pass of the plasma torch across the substrate. Typically, temperatures up to 500 °C

were measured from the substrates during the raster scan deposition and about 700 °C in multiple single scan deposition. The third set of experiments involved the collection of deposits for a single scan of the plasma torch across a preheated, polished (1 μm finish) substrate. The latter set of experiments was performed in order to collect and analyze individual splats.

2.3 Measurement of Solution Precursor Properties

The thermal characteristics of the precursors were analyzed by drying the precursor solutions in a low-temperature muffle furnace preheated to 120 °C for about 15 h; during this process, the solutions were converted to gels. Samples of the dried gels were evaluated using a combined TGA-DSC instrument (SDT-Q6000 thermal analyzer, TA Inc., New Castle, DE), in which thermogravimetric and calorimetric data are obtained simultaneously from the same sample in flowing N₂ atmosphere. For each thermal analysis run, about 15 mg of dried precursor gel was placed in a sample pan made of Al₂O₃. The analyses were performed by heating each sample from room temperature to 1000 °C at a rate of 10 °C/min with N₂ flow rate of 100 mL/min.

The surface tension of the precursor solutions was measured using a dynamic contact angle analyzer (Thermo Cahn Instruments, Madison, WI). This makes use of the Wilhelmy plate technique in which the equilibrated forces on a microscope slide immersed in the solution precursor sample was measured.

The viscosity of the solutions was measured using a Ubbelohde type viscometer, No. 1 (Cannon Instrument Company, State College, PA) in a temperature-controlled bath.

2.4 Synthesis of Oxide Particles from Solution Precursors

Oxide particles were produced from the thermal decomposition of the precursor solutions in a muffle furnace. This was carried out in a two-step process that involved the drying (at 120 °C for 15 h) of the precursor solution in a beaker and then the calcining (at 500 °C for 2 h) of the dried precursor. The densities of the oxide particles were obtained from the Brunauer-Emmet-Teller (BET) particle analysis of the residues resulting from the thermal decomposition process. The BET particle analysis procedure was carried out on a Gas Sorption Analyzer (NOVA 1000, Quantachrome instruments) with nitrogen gas as the adsorbate. For convenience, we will refer to the

oxide particles synthesized by this process as “furnace-pyrolyzed particles.”

2.5 Characterization of Deposited Coatings and Particles

The deposited coatings were characterized by XRD using Cu K_{α} radiation in a high-resolution powder diffractometer (D5005; Bruker AXS, Karlsruhe, Germany). The XRD spectra were acquired by scanning over the angular range $2\theta = 5^{\circ}$ to 90° at a scan speed of $5^{\circ}/\text{min}$. The scan was repeated until the statistical noise in the spectra was reduced to the point where all of the peaks could be distinguished clearly; this typically required about 20 scans for a total scan time of about 6 h.

The morphologies of the coatings were examined from polished cross sections using an environmental scanning electron microscope (ESEM 2020, Philips Electron Optics, Eindhoven, the Netherlands). Focused ion beam (FIB) sectioning with a combination of scanning electron microscopy (SEM) and transmission electron microscopy (TEM) imaging were also used to observe the microstructure and morphology of the coatings and particles synthesized from the solution precursors, as well as to investigate the coating architecture and the distribution and evolution of grain sizes and phase domains within the coatings. The FIB sectioning was performed in a FEI Strata 400S Dual-Beam instrument (FEI Company, Hillsboro, OR) equipped with high-resolution electron and Ga^{+} ion beam columns and the TEM characterization was carried out on an FEI Tecnai T12 TEM (FEI Company, Hillsboro, OR), equipped with an EDAX r-TEM energy dispersive x-ray spectrometer (EDXS), and operating at an accelerating voltage of 120 kV. Cross-sectional TEM samples were prepared using the Dual-Beam FIB. Details of the sample preparation procedure using the FIB are reported elsewhere (Ref 24). Coating porosity was estimated from the polished cross sections by image analysis. The Vickers hardness (HV) was also measured on the polished cross sections with a 0.98 N normal load and a dwell time of 15 s. In each case, the hardness value was taken to be the average of five measurements.

3. Results

In order to better understand the effect of various factors on SPPS deposition, data has been collected on the following: (1) physical properties of precursors—viscosity, surface tension, and molarity; (2) thermal properties of precursors, e.g., mechanism of thermal decomposition and precursor reaction energetics; (3) decomposition products (especially the density of the oxide particles); and (4) the influence of the precursor chemistry on coating microstructure. Although not strictly part of the results, the reader should note that the size and density of the particles in the plasma stream determines the ability of the particles to deposit on the substrate (Stokes number effect) (Ref 25). Larger and denser particles are better

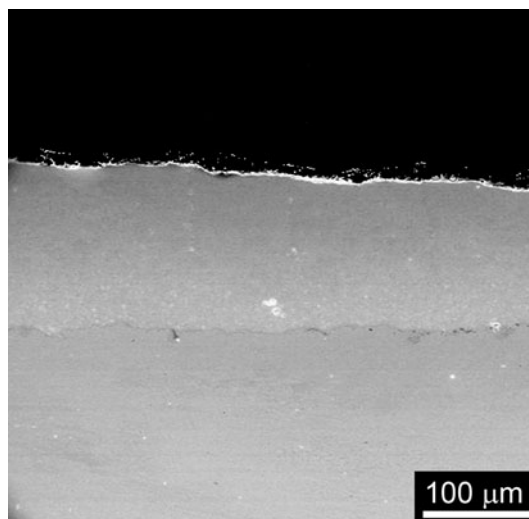


Fig. 2 Cross-sectional SEM image of 7YSZ coating obtained from the plasma spraying of zirconium acetate-based precursor solution

able to deposit on the substrate, and at near normal incidence. Porosity in the pyrolyzed particles often ends up in the final coating. Finally, we note that the YSZ precursor solution produces very dense coatings, an example of which is shown in Fig. 2. Therefore, comparisons will be made between Y_2O_3 and MgO precursors and those of YSZ to guide the ongoing efforts to make dense Y_2O_3 -MgO nanocomposites.

3.1 Precursor Properties

Several properties of the various precursor solutions investigated in this study were measured. The properties related to the solubility of the precursors were measured and are shown in Table 2, while the measured values of the fluid and thermal properties are shown in Table 3. The theoretical mass and diameter of the furnace-pyrolyzed oxide particles, based on BET measured density (Table 2), are calculated and shown in Table 4.

3.2 Thermal Characteristics of Precursors

A very significant amount of heat energy can be added to, or absorbed from, the plasma jet during the SPPS process as a result of the pyrolysis of the injected precursor solution. This phenomenon does not occur in the APS and SPS processes and constitutes a major difference between the SPPS process and these other plasma spray processes. However, this aspect of SPPS has rarely been discussed. Considering the fact that a typical ceramic has a specific heat of about 0.5 J/g, the energy released during the pyrolysis of precursors that decompose exothermically has the potential to heat the resulting pyrolyzed particles by hundreds of degrees Celsius. Figure 3 shows the DSC measurements of heat flow for the five precursors used in this study. Table 3 shows the net heat gain or loss for each precursor and, as noted, these energies can be associated with significant temperature changes.

Table 2 Properties of various Y_2O_3 -MgO precursor solutions compared with those of YSZ

Precursor type notation	Precursor salts	Vol. $H_2O/100$ g of salt mixture, ml	Molarity, mol/L	Solution density, g/cm^3	Oxides/liter of solution, g	Particle density, g/cm^3
Y[n]Mg[n]	$Y(NO_3)_3 \cdot 6H_2O$ $Mg(NO_3)_2 \cdot 6H_2O$	125	2.77	1.27	179	1.52
Y[a]Mg[a]	$Y(C_2H_3O_2)_3 \cdot 4H_2O$ $Mg(C_2H_3O_2)_2 \cdot 4H_2O$	680	0.53	1.05	34	3.31
Y[a]Mg[a] *Heated	$Y(C_2H_3O_2)_3 \cdot 4H_2O$ $Mg(C_2H_3O_2)_2 \cdot 4H_2O$	152	2.37	1.20	156	3.31
Y[n]Mg[a]	$Y(NO_3)_3 \cdot 6H_2O$ $Mg(C_2H_3O_2)_2 \cdot 4H_2O$	470	0.76	1.03	49	1.25
Y[n]Mg[a] *Heated	$Y(NO_3)_3 \cdot 6H_2O$ $Mg(C_2H_3O_2)_2 \cdot 4H_2O$	140	2.55	1.18	165	1.25
Y[n]Mg[n] + NH_4 [a]	$Y(NO_3)_3 \cdot 6H_2O$ $Mg(NO_3)_2 \cdot 6H_2O$ $NH_4(C_2H_3O_2)$	135	3.20	1.28	160	1.46
YSZ	$Zr(CH_3COO)_4$ $Y(NO_3)_3 \cdot 6H_2O$	N/A	2.53	1.33	310	5.2

*Precursor solution was prepared at 90 °C

Table 3 Fluid and thermal properties of various Y_2O_3 -MgO precursor solutions compared with those of YSZ

Precursor type	Viscosity, mPa s	Surface tension, mN/m	Exothermic heat, J/g	Endothermic heat, J/g^{-1}	Net heat, J/g
Y[n]Mg[n]	2.26	46.51	0	-472.2	-472.2
Y[a]Mg[a]	1.24	48.54	0	-477.1	-477.1
Y[n]Mg[a]	1.43	66.40	722.0	-191.1	530.9
Y[n]Mg[n] + NH_4 [a]	2.30	50.34	402.0	-175.5	226.5
YSZ	6.16	52.65	419.1	-33.4	385.7

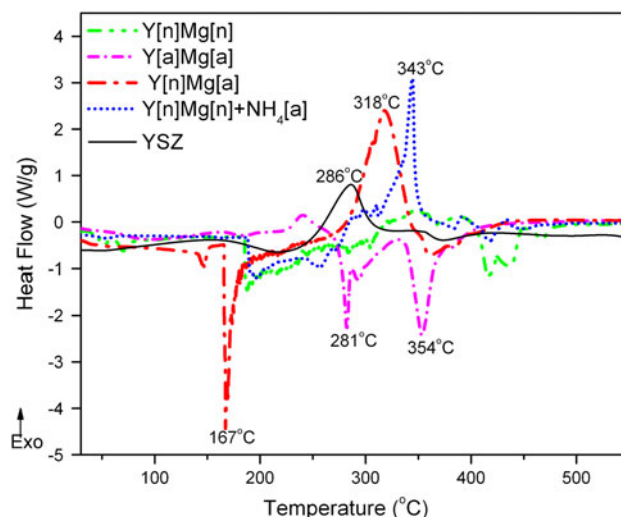
Heat = heat of decomposition reaction

Table 4 Estimated mass and size of a particle produced from the thermal decomposition of a 40 μm precursor droplet

Precursor	40 μm droplet on pyrolysis	
	Mass ($\times 10^{-9}$ g)	Diameter, μm
Y[n]Mg[n]	6.0	19.6
Y[a]Mg[a]	1.2	8.7
Y[a]Mg[a] (heated)	5.2	14.4
Y[n]Mg[a]	1.7	13.6
Y[n]Mg[a] (heated)	5.5	20.4
Y[n]Mg[n] + NH_4 [a]	5.4	19.1
YSZ	10.4	15.2

3.3 Characteristics of Particles Generated as a Function of Precursor Type

The weights of oxide particles shown in Table 4 were calculated based on the assumption that the solution droplet in each case leaves a nondisintegrated oxide residue after the pyrolysis of the precursor salts. However, it has been observed that the characteristics of the oxide particles produced from a solution precursor vary with the precursor content (Ref 24, 26). Evidence for such differences could be observed visually as shown in Fig. 4 and detailed information about the particle morphology was obtained using SEM. SEM images of the furnace-pyrolyzed particles produced by the thermal

**Fig. 3** Plots of DSC heat flow data obtained at a heating rate of 10 °C/min from various Y_2O_3 -MgO precursor mixtures and YSZ precursor

decomposition of the various Y_2O_3 -MgO precursor solutions examined in this study are shown in Fig. 5(a)-(d). These particles were affixed to double-sided carbon tape on a standard SEM stub before loading into the microscope. The insets are cross-sectional views through the agglomerated particles milled using the FIB; these

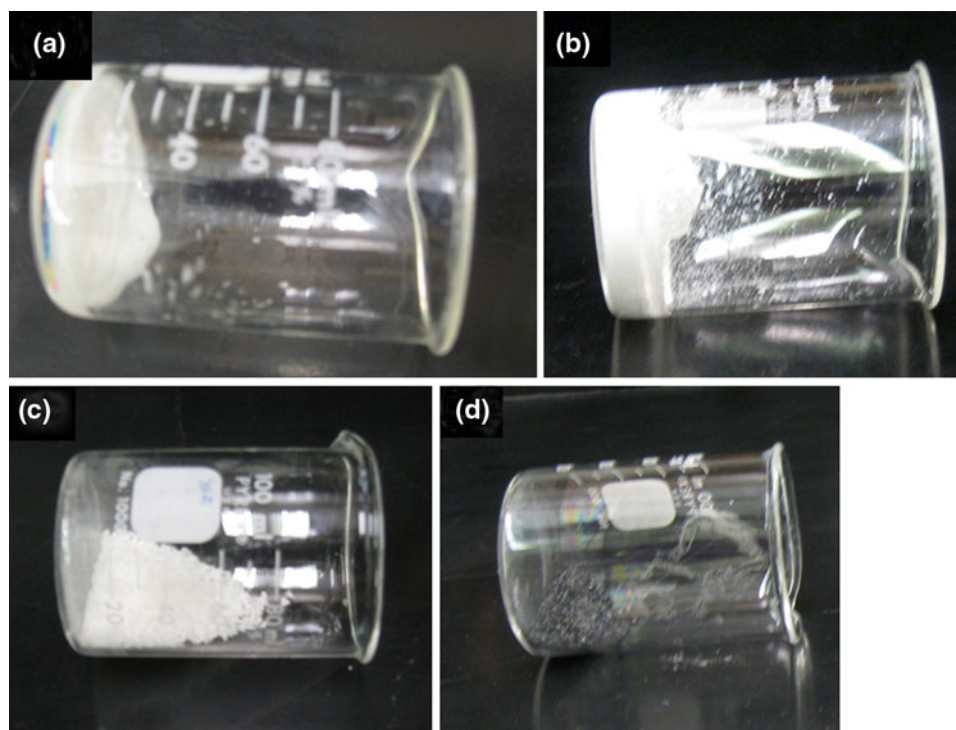


Fig. 4 Appearance of unpyrolyzed and furnace-pyrolyzed materials (a) and (b) unpyrolyzed Y[n]Mg[n] precursor and furnace-pyrolyzed Y₂O₃-MgO particles, respectively; (c) and (d) unpyrolyzed YSZ precursor and furnace-pyrolyzed YSZ particles, respectively

sections reveal the packing structure and internal morphology of the agglomerates produced from each precursor solution. The oxide particles produced from the Y[n]Mg[n] and Y[a]Mg[a] precursor solutions were in form of lumps (Fig. 5a and b, respectively). An FIB-milled section through the lumps (insets) revealed that the particles from the Y[n]Mg[n] mixture were in form of hollow agglomerates. In contrast to this, the material from the Y[a]Mg[a] mixture does not exhibit such a hollow structure and instead contains only distributed pores. Thus, on the length scales considered here, the material shown in Fig. 5(a) is more porous (i.e., lower overall density) than that shown in Fig. 5(b). However, the precursor solutions containing a combination of Y[n] and Mg[a] produced finer particles that were flaky, friable, and easily airborne (Fig. 5c). With the addition of some NH₄[a] to the Y[n]Mg[n] mixture, the morphology and packing structure of the oxide particles produced on thermal decomposition of the resultant solution changed from large porous lumps (measuring up to 10 mm) to finer agglomerates (<0.4 mm), as shown in Fig. 5(d). The size of the agglomerates became much smaller as the quantity of the NH₄[a] was increased.

The corresponding morphology of the YSZ particles formed by the thermal decomposition of the YSZ precursor solution is shown in Fig. 6. Unlike the porous and loosely agglomerated particles formed from the Y₂O₃-MgO precursor solutions, the YSZ particles (<2.5 mm) were dense, hard, and exhibited a more uniform size distribution.

3.4 Coating Structure and Precursor Chemistry

Examples of cross-sectional SEM images from coatings obtained by SPPS using the various Y₂O₃-MgO precursor solutions investigated in this study are shown in Fig. 7(a)-(d). A seemingly columnar-type microstructure was observed for the coatings deposited from the Y[n]Mg[n] precursor solution as revealed in Fig. 7(a). The coating deposited from the Y[n]Mg[a] precursor solution at room temperature, using the same process parameters, was relatively thin (Fig. 7c) owing to the low solute loading of this solution as a result of the limited solubility of the salt mixture at room temperature. The inset in Fig. 7(c) shows a corresponding cross-sectional SEM image of the coating deposited from heated Y[n]Mg[a] precursor solution, which also appears very porous and columnar. The Y[a]Mg[a] precursor solution was also sprayed hot due to solubility issues; the coating obtained from this precursor mixture also exhibited some porosity (Fig. 7b), but this porosity was more randomly distributed and did not form columns. In contrast, a relatively dense microstructure was observed for the coating deposited from the Y[n]Mg[n] solution containing some NH₄[a]; the regions adjacent to the substrate had some crack-like porosity, while the top of the coating appeared very dense (Fig. 7d).

The porosity observed on the mechanically polished coating cross sections, as shown in the images in Fig. 7, is usually more than the actual porosity present in the as-sprayed coatings. This could be attributed to the “pull-out” of loosely bonded particles during the mechanical

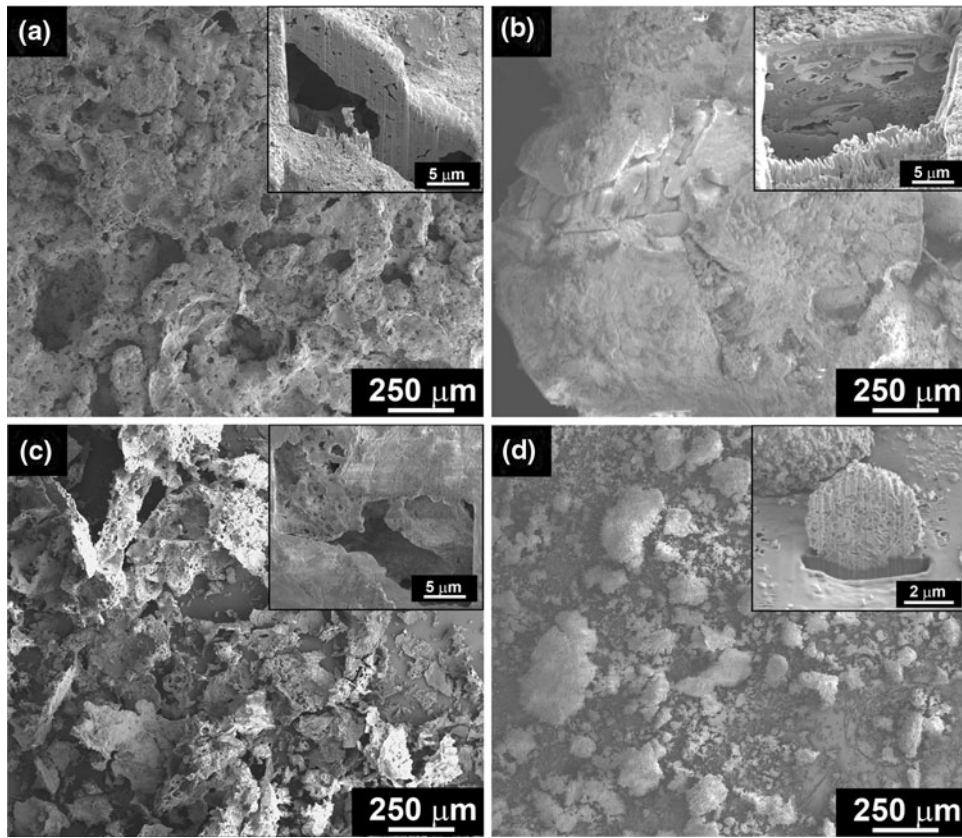


Fig. 5 SEM images of the particles produced by the thermal decomposition of the various Y_2O_3 -MgO precursor solutions (a) $Y[n]Mg[n]$, (b) $Y[a]Mg[a]$, (c) $Y[n]Mg[a]$, and (d) $Y[n]Mg[n] + NH_4[a]$. The inset is the side view of a section through the agglomerated particles milled using the FIB

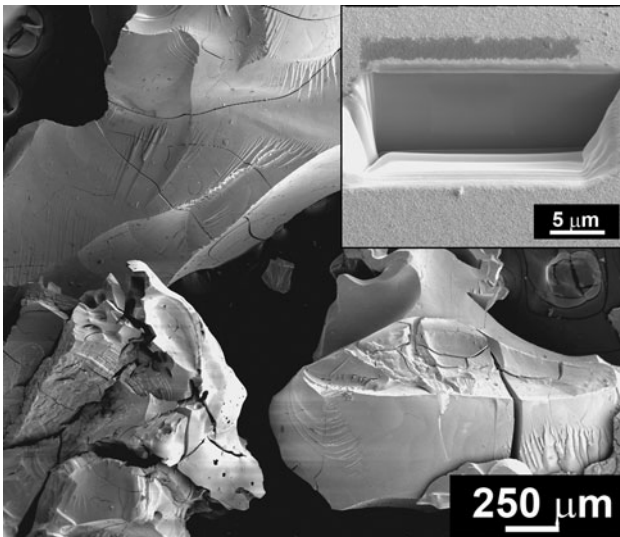


Fig. 6 SEM images of the YSZ particles produced by the thermal decomposition of zirconium acetate-based precursor solution. The inset is the side view of a section through the agglomerated particles milled using the FIB

polishing step of the sample preparation process. In order to obtain a true representation of the porosity, a trench was milled in the coating using the FIB, and the wall of the trench was imaged. Figure 8(a)-(d) are SEM images of the walls for such FIB-milled trenches in the coatings produced from the $Y[n]Mg[n]$, $Y[a]Mg[a]$, $Y[n]Mg[a]$, and $Y[n]Mg[n] + NH_4[a]$ precursor solutions, respectively. The wall of the trench in the coatings deposited from the $Y[n]Mg[n]$ and $Y[n]Mg[a]$ solutions exhibited the least dense structures, which is consistent with the observation from the mechanically polished samples. However, the level of porosity observed in the images of the trench walls is lower than that observed in the mechanically polished samples, and the columnar structure is less clearly defined. It is important to point out that coatings deposited by some other processes such as electron beam physical vapor deposition (EB-PVD) and chemical vapor deposition (CVD) processes, typically exhibit this sort of columnar microstructure where elongated intercolumnar pores become predominantly aligned perpendicular to the plane of the coating as the thickness increases (Ref 27-29). Plasma deposited coatings, on the other hand, are not usually characterized by columnar structure, although

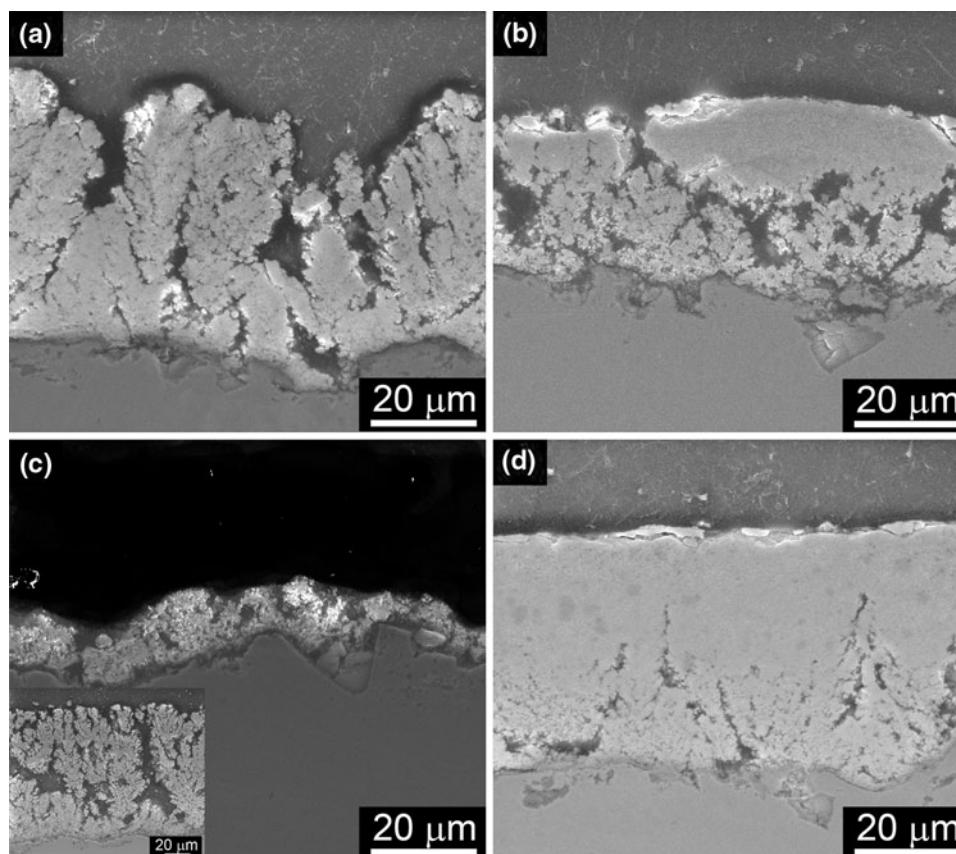


Fig. 7 Cross-sectional SEM images of Y_2O_3 -MgO coatings obtained from the plasma spraying of four different precursor solutions (a) $Y[n]Mg[n]$, (b) $Y[a]Mg[a]$, (c) $Y[n]Mg[a]$, and (d) $Y[n]Mg[n] + NH_4[a]$. The inset in (c) is a corresponding cross-sectional SEM image of a coating obtained from a heated $Y[n]Mg[a]$ precursor solution

columnar alignment of porosity has been observed under certain circumstances (e.g., Ref 30): this was linked to shadowing effects induced by substrate surface topography but further work is required to establish if this is the cause in our materials. In the plasma deposition process, unmelted particles are typically trapped in the coating lamellae; these are particles that are too fine to be entrained in the hottest core of the plasma jet or are too large to be melted within the short residence time of the particle in the jet. These unmelted particles tend to pull-out during metallographic polishing to create additional porosity in the cross-sectioned surface. Thus, the extent of the “pull-out” could be a metric for the degree of melting of the particles during the spraying process. Since these unmelted particles would tend to be concentrated in the more porous regions within a columnar structure, one might expect pull-out effects to make this structure more evident in mechanically polished sections than in FIB-cut sections as observed experimentally.

The coating obtained from the $Y[n]Mg[n] + NH_4[a]$ precursor solution appeared very dense as revealed by the image of the FIB-milled trench wall (Fig. 8d), while that obtained from the $Y[a]Mg[a]$ solution (Fig. 8b) had both dense regions and porous regions. This indicates that the particles resulting from the pyrolysis of the former precursor solution in the plasma jet experienced more melting

than the corresponding particles from the latter solution. The average hardness values of these coatings also showed some correlation with the density observed from the SEM images. The coating deposited from the $Y[n]Mg[n] + NH_4[a]$ precursor solution gave the highest hardness value of ~ 560 HV, while the coating obtained from the $Y[a]Mg[a]$ solution had a hardness of ~ 380 HV. The hardness values for the coatings deposited from the $Y[n]Mg[n]$ and $Y[n]Mg[a]$ solutions were ~ 190 and 110 HV, respectively.

3.5 Phase and Grain Structure of Multiscan Deposits

From the XRD data shown in Fig. 9, it is seen that the crystal structures of the resultant phases in the Y_2O_3 -MgO composites deposited by SPPS are not influenced by the chemistries of the solution precursor mixtures from which they were produced. In each case, the XRD peaks correspond to those expected for the cubic bixbyite polymorph of Y_2O_3 and the NaCl-type structure of MgO. However, the sizes, morphologies, and distributions of the grains and phase domains appear to vary slightly with the precursor solution, as shown by the bright field (BF) TEM images in Fig. 10(a)-(d). This is consistent with our previous results on the structural characteristics of Y_2O_3 -MgO composites

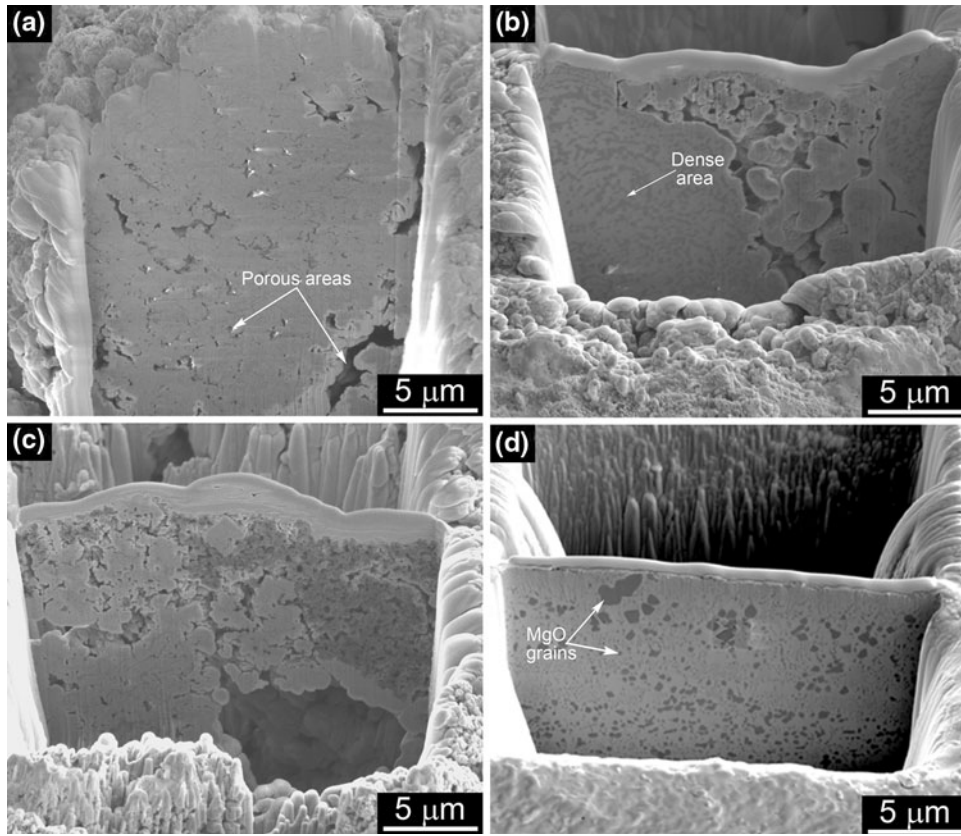


Fig. 8 SEM images (secondary electrons) of the wall of FIB-milled trenches in the Y_2O_3 -MgO coatings produced from four different precursor solution (a) $Y[n]Mg[n]$, (b) $Y[a]Mg[a]$, (c) $Y[n]Mg[a]$, and (d) $Y[n]Mg[n] + NH_4[a]$

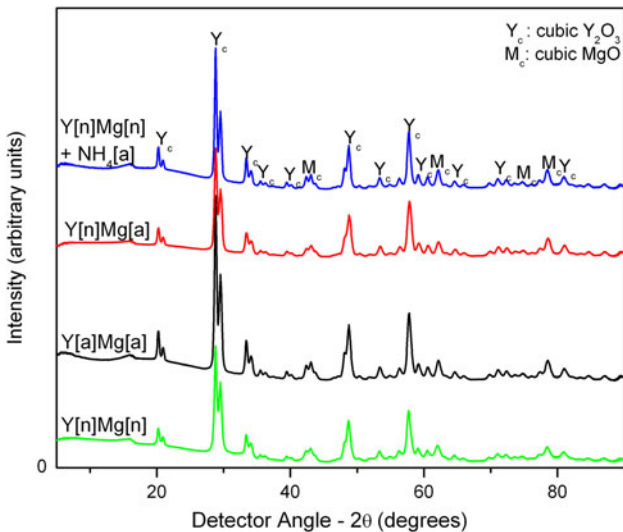


Fig. 9 XRD spectra obtained from coatings deposited from different precursor solutions as indicated

synthesized by a combined sol-gel/thermal decomposition route using similar precursor solutions (Ref 24). The Y_2O_3 and MgO grains in the deposits from the $Y[n]Mg[n]$ and $Y[n]Mg[a]$ solutions appear to be smaller than the

corresponding grains in the materials deposited from the other two precursor solutions. This discrepancy is more prominent in the MgO grains which have an average diameter of slightly above 100 nm in the deposits obtained from the $Y[n]Mg[n]$ and $Y[n]Mg[a]$ solutions and ~400 nm in the deposits from the $Y[a]Mg[a]$ and $Y[n]Mg[n] + NH_4[a]$ precursor solutions. This difference may be due to greater melting of the particles in the latter deposits.

The deposits obtained from the $Y[n]Mg[n] + NH_4[a]$ precursor solution exhibited an alternating layer structure of coarse and fine grains of both Y_2O_3 and MgO as shown in Fig. 11(a). The fine-grained layers comprised elongated grains (<100 nm across) resembling a lamellar-type eutectic microstructure (Fig. 11b), while the coarser-grained layers exhibited more equiaxed grains with diameters of up to 400 nm.

3.6 Structure of Single Scan Deposits

Single scan deposits produced using the $Y[a]Mg[a]$ solution precursor were collected on a polished substrate and the electron microscopy data is shown in Fig. 12. A FIB-milled cross section was made through a splat (Fig. 12a) to reveal the morphology and distribution of the phases in the splat, as well as the degree of contact at the splat/substrate interface. The TEM data in Fig. 12(b) reveal that the splat consists of both amorphous and

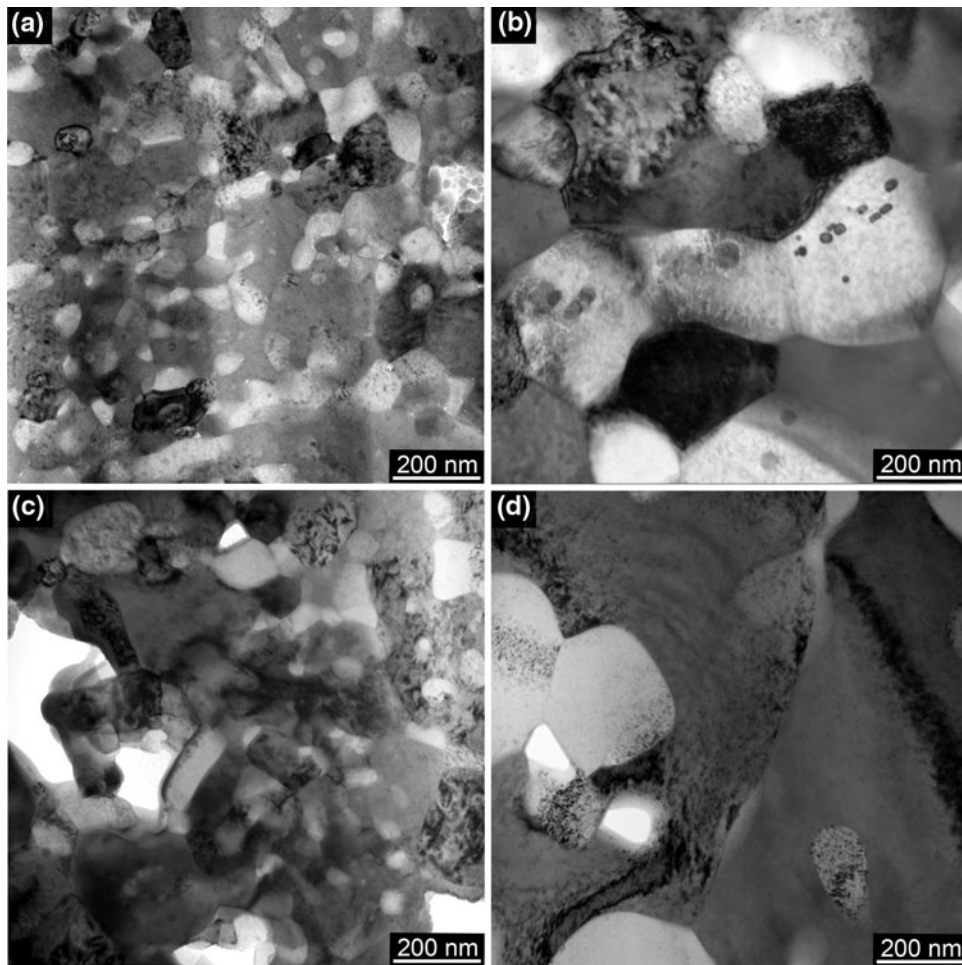
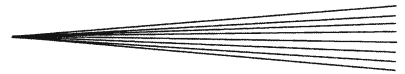


Fig. 10 BF TEM images from FIB-cut thin sections of Y_2O_3 -MgO coatings showing the grains of the component phases (darker grains are mostly Y_2O_3 although some MgO grains may appear dark due to diffraction contrast effects). The coatings were produced from four different precursor solution (a) Y[n]Mg[n], (b) Y[a]Mg[a], (c) Y[n]Mg[a], and (d) Y[n]Mg[n] + NH_4 [a]

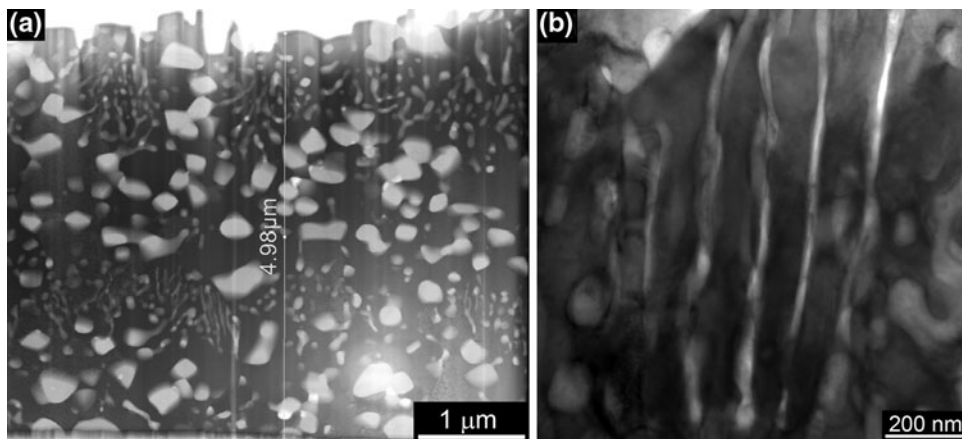


Fig. 11 BF TEM images from FIB-cut thin sections of Y_2O_3 -MgO coating produced from the Y[n]Mg[n] + NH_4 [a] precursor solution. (a) Lower magnification image showing the alternating large and small grain regions; (b) higher magnification image of the small grain region showing a eutectic-like structure

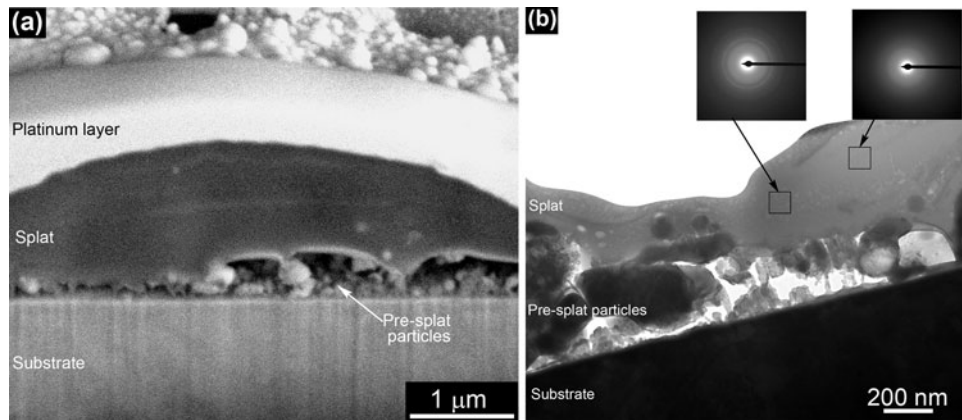


Fig. 12 Electron microscopy data from the materials deposited in a single scan spray using the Y[a]Mg[a] precursor solution. (a) SEM image (backscattered electrons) of a FIB-milled cross section through a splat; (b) BF TEM image from a FIB-cut thin section. The insets are diffraction patterns from the areas indicated

crystalline areas as shown by the inset diffraction patterns. The grains within the crystalline regions are <10 nm in diameter. The interface between the splat and the substrate was found to contain many crystalline particles which appear to be unmelted.

4. Discussion

Conventional APS processes using powdered materials are complex, and are affected by many interacting variables. The use of SPS introduces additional variables, including droplet break-up, and the energetics and kinetics of solvent evaporation. The same issues found in APS and SPS spraying are also important for the SPPS process but there are further potentially complicating factors that must be considered. In the case of SPPS, some of the controlling factors for obtaining dense deposits are just now being identified. In this article, we consider solution molarity (Ref 31), the energetics of the chemical reactions in the solution, and the physical form of the reaction by-product (especially density). In light of this complexity, and to highlight the characteristics needed to make a dense SPPS coating, the current experiments were conducted to compare the properties of our best-behaved precursor (the Zr[a]-based precursor for YSZ) with the properties for precursors that have not produced such dense coatings and that have lower deposition efficiencies.

The size and density of reaction products in the plasma stream play a critical role, as will now be discussed. A mixture of gas and ceramic particles arrives at the substrate. The gas cannot pass through the substrate and will turn and flow along the flat substrate and off the edge. If a particle is too small and/or of low density, it will follow the gas stream and either not impinge on the substrate at all or it will deposit at an oblique angle. This phenomenon can contribute to the porosity of the coatings deposited using precursors that form small and/or low density particles on pyrolysis (e.g., Y[n]Mg[a]). There is also evidence that thermophoretic forces can push very small particles to the

periphery of the plume, where temperatures are lower and melting is unlikely (Ref 32). In a simple case, one can consider the Stokes number, which contains the square of the particle diameter multiplied by the density (Ref 33). Small and/or low density particles are therefore difficult to deposit. In addition, porosity in an arriving particle can end up in the coating if there is partial melting or if trapped gas in the pores cannot escape. This effect is sometimes evident in the deposition of hollow spherical powder (HOSPTM), rather than fused and crushed powder, in conventional plasma spray (Ref 34). Consequently, precursors leading to low density and/or to small particles are likely to be poor candidates for making dense coatings.

4.1 Precursor Properties

The fluid properties of the five precursor solutions investigated in this study are presented in Table 3. The surface tension of all five solutions is very similar, but the YSZ precursor has a significantly higher viscosity. While solution viscosity may influence the behavior during SPPS by, for example, improving entrainment (Ref 31, 35), however, recent studies have suggested surface tension is far more important than viscosity (Ref 35). Thus, viscosity was not investigated further as the primary source of the superior spray performance for the YSZ precursors in this work. Another factor to be considered is the solubility of the salts used in the precursor solution; this determines the upper limit of the molarity for the solution obtained. In earlier work on our YSZ precursor, it was shown that as molarity is increased, the coating density and quality improved (Ref 31). Table 2 shows the molarity and the equivalent mass of oxide contained in a liter of solution for the various precursors used in this study. In order to obtain a molarity in the Y₂O₃-MgO precursor solutions that was comparable to that of the YSZ precursor solution, it was necessary to heat the solvent to about 90 °C (particularly for the precursor mixtures containing a metal acetate salt). A delivery system for injecting such heated precursor solutions into the plasma jet was developed. The densities of the coatings obtained from spraying the

Y_2O_3 -MgO precursor solutions (Fig. 7) were a lot lower than that of the YSZ coatings (Fig. 2), even though the solutions had similar molarities. This suggests that a high molarity precursor solution is a necessary but not sufficient condition for the deposition of dense coatings in the SPPS process.

The YSZ precursor solution, however, does have the highest equivalent mass of oxide per liter of solution by nearly a factor of 2, due to the absence of large amounts of volatile materials (e.g., hydrated water) in Zr[a]. These volatile materials are released during precursor pyrolysis and can result in a lower particle temperature and oxide yield if they are present in large quantities. To clarify this issue further, Table 4 shows the expected size of the oxide particles resulting from 40 μm precursor droplets, based on the stoichiometry of the liquid and the end point density measured using BET on furnace-pyrolyzed precursor (Table 2). The expected size of the YSZ particles falls within the range of those for the other precursor mixtures, but the expected density is significantly higher. Additional data supporting the density advantage of the YSZ precursor and corroborating the BET data can be seen by comparing the furnace-pyrolyzed material obtained from the YSZ precursor (Fig. 5) to the materials obtained from the four different Y_2O_3 -MgO precursors using the same pyrolysis process (Fig. 4). From the morphology of these latter materials, it would be expected that the particles would be highly susceptible to further break-up in the plasma jet. Thus, these fragmented particles would have the disadvantages of both low density and small size, reducing their chances of being deposited on the substrate due to the Stokes Number effect. This particle density difference appears to be the most important factor accounting for the denser structure observed in the coatings produced from the YSZ precursor solution (Fig. 2). It would appear that the use of the BET method to measure the density of furnace-pyrolyzed particles is a good screening tool for precursor selection for the SPPS process. An even simpler method that has worked well for us so far is observation of the apparent density of pyrolyzed materials with the naked eye. For example, the density differences between the unpyrolyzed and furnace-pyrolyzed materials from the $Y[n]Mg[n]$ and YSZ precursor solutions are readily apparent in the images presented in Fig. 4.

4.2 Thermal Characteristics of the Precursors

A unique phenomenon in the SPPS process is the chemical reactions which occur during the spray process as the injected precursors undergo pyrolysis in the plasma jet. This results in the release or absorption of heat energy which can have a great influence on the particle temperature of the plasma. The DSC data reported here (Fig. 3) can be used to extract the total energy released or absorbed in the chemical reactions that occur. Table 3 shows the net energy from these reactions. As can be seen energies up to 722 J/g are involved. To put this in context, consider the fact that ceramics typically have specific heats of about 0.5 J/g. As such, the heat energy released during

an exothermic reaction could, in principle, raise the temperatures of the materials by hundreds of degrees Celsius. It is clear that the YSZ precursor is not the one that decomposes most exothermically. However, in Fig. 3, it can be seen that all of the other precursors undergo significant endothermic processes in the early stages of heating. This endothermic behavior is expected to be particularly significant in SPPS because the material is traveling in a plasma jet, which is dropping rapidly in temperature. Endothermic behavior at low temperatures will delay particle heating and pushing the location where the melting point is reached down stream. At a critical location downstream the gas temperatures drops below the melting point and particles not melted by then will never melt preventing the entrained material from reaching the appropriate melting temperature. It is, therefore, clearly undesirable for an SPPS precursor solution to undergo endothermic reactions. All of the Y_2O_3 -MgO precursor solutions undergo endothermic reactions, whereas the YSZ precursor does not; this is consistent with the idea that the endothermic reactions may contribute to the inferior spray performance of the Y_2O_3 -MgO precursor solutions. In a later section, we will discuss the way in which these concerns might be addressed by adding combustible chemicals to the precursor to make the overall process more exothermic.

4.3 Particle Morphology and Precursor Properties

The observed variation in size, morphology, and packing structure of the particles produced from these precursor solutions may be associated with the characteristics of the individual salts contained in the solution and the decomposition mechanism of the precursor mixture. The yttrium and magnesium salts used in the Y_2O_3 -MgO precursor solutions are all hydrated. Such salts tend to melt in their water of crystallization at relatively low temperatures (mostly $<100^\circ\text{C}$) forming a clear viscous mass. This may lead to the formation of sticky viscous droplets (blobs) during the precursor spraying, resulting in low heat transfer to the droplets because of the large size and the extra energy or time needed to remove water of hydration. Such blobs are sometimes deposited on the substrate as unpyrolyzed materials or pyrolyzed but unmelted particles, both of which are deleterious to the deposition of dense coatings.

The characteristics of the oxide particles produced from precursor solutions can also be significantly affected by the thermal decomposition mechanism (endothermic or exothermic) inherent in the precursor mixture. Thermal decomposition reactions that occur endothermically are usually sluggish since absorption of heat is required to drive the decomposition process. This leads to a slow release of decomposition gases from the precursor mixture during the pyrolysis process to form large oxide particles in a porous network. Exothermic reactions, however, tend to be fast and vigorous due to the combustion process resulting from the redox reaction between the oxidizer and the reducer (fuel) during the decomposition. The rate and degree of combustion, as well as the heat evolved

during the process, depend on the relative amounts of the oxidizer and the reducer in the precursor mixture. This also controls how suddenly the decomposition gases are released, which influences the characteristics of the oxide particles produced. Mixtures containing stoichiometric quantities of oxidizers and reducers have been observed to undergo the maximum rates of combustion during the thermal decomposition process to produce very fine oxide particles. This may not be advantageous in the SPPS process, since the vigorous/explosive reaction may throw most of the fine oxide particles out of the hotter core of the plasma jet. The heat released from an exothermic decomposition, however, could add to the enthalpy of the jet, thereby increasing the thermal treatment of the particles in the plasma jet. There is then an optimal exothermicity for a precursor mixture. The addition of 50% of the stoichiometric amount of $\text{NH}_4[\text{a}]$ to the $\text{Y}[\text{n}]\text{M}[\text{n}]$ precursor solution allows for the sustenance of the exothermic reaction during the decomposition process and the formation of moderately disintegrated particles. This resulted in improved coating density as described in the next section.

4.4 Coating Structure and Precursor Chemistry

In section 3.4, mechanically polished and FIB-cut cross sections were compared, and it was shown that weakly bonded or semipyrolyzed materials are removed during polishing, leaving the melted harder structure behind. A comparison of the polished sections in Fig. 7(a)-(d) show that the densest coating was produced using the $\text{Y}[\text{n}]\text{Mg}[\text{n}] + \text{NH}_4[\text{a}]$ precursor solution. When a solution precursor is injected into the plasma jet, various phenomena can occur which determine the state of the particles deposited on the substrate, thus affecting the properties of the resultant coatings. Particles in the molten state form splats on impact while the unmelted particles are either trapped in the splats, adhere loosely to the substrate, or simply bounce off. The formation of dense coatings involves the layering of splats with little or no entrapment of unmelted particles. The microstructure of a coating obtained in the SPPS process will be determined by the degree of melting of the particles. This degree of melting may be affected by precursor solution properties including solution concentration, thermal decomposition characteristics of the precursor salt mixture, and the characteristics of the oxide particles formed on pyrolysis. In addition, process parameters such as injected precursor momentum, plasma jet interaction and heat transfer, flight trajectory and residence time of droplets/particles in the plasma, and substrate temperature, can also affect the microstructure of the coatings deposited in the SPPS process.

The relatively high density of the coating deposited using the $\text{Y}[\text{n}]\text{Mg}[\text{n}] + \text{NH}_4[\text{a}]$ precursor solution can be attributed to a combination of two factors: (i) the exothermic decomposition characteristics of the precursor (Fig. 3) and (ii) the formation of oxide particles which are not too flakey or fluffy to remain entrained in the core of the plasma jet (Fig. 4). Exothermic decomposition characteristics are important for SPPS precursor solutions.

The thermal decomposition of an exothermic precursor mixture tends to be faster than the decomposition of an endothermic mixture such as the $\text{Y}[\text{n}]\text{Mg}[\text{n}]$ precursor. The reducing salt, which acts as a fuel during the decomposition process, undergoes a redox reaction with the oxidizing salt at a certain temperature leading to a fast combustion reaction. This will lead to the early formation of the oxides thereby increasing the residence time of the oxide particles in the plasma jet. Moreover, there will be an adiabatic temperature rise associated with the exothermic decomposition process which results from the heat released from the combustion reaction. This will increase the enthalpy available in the plasma jet to melt the oxide particles.

Even though the $\text{Y}[\text{n}]\text{Mg}[\text{a}]$ solution precursor has similar decomposition characteristics to the $\text{Y}[\text{n}]\text{Mg}[\text{n}] + \text{NH}_4[\text{a}]$ solution, the morphology of the oxide particles formed was rather different. The particles formed on decomposition of the $\text{Y}[\text{n}]\text{Mg}[\text{a}]$ mixture were flaky, fluffy, and easily airborne. Such particles will tend to be carried along the colder periphery of the plasma jet during the spray process, thus achieving little or no melting. This may account for the huge difference in the density of the coatings deposited using the two different precursor solutions. The $\text{Y}[\text{a}]\text{Mg}[\text{a}]$ precursor mixture decomposes endothermically in an inert atmosphere, like the $\text{Y}[\text{n}]\text{Mg}[\text{n}]$ mixture, but the oxide particles formed are denser (Fig. 4). Such particles would be entrained more effectively in the plasma jet resulting in more melting of these particles than those from the $\text{Y}[\text{n}]\text{Mg}[\text{n}]$ mixture. However, because of the sluggish endothermic decomposition characteristics of the $\text{Y}[\text{a}]\text{Mg}[\text{a}]$ precursor, the coatings formed are not very dense. Thus, it would appear that the deposition of a dense coating via the SPPS process would require a precursor mixture that decomposes exothermically and that this decomposition results in the formation of dense particles.

In all cases, increasing the concentration of the solution increased the density of the coating obtained up to a certain limit, after which further increases in concentration either led to clogging of the injection nozzle or to over-penetration of the droplets (if the injection pressure is increased to prevent the clogging), both of which resulted in the deterioration of the coating density.

4.5 Resulting Phase Composition

The crystalline phases formed are the same for all of the Y_2O_3 -MgO precursors mixtures used in this study (Fig. 9). The deposits obtained from the $\text{Y}[\text{n}]\text{Mg}[\text{n}] + \text{NH}_4[\text{a}]$ precursor solution exhibited an alternating layer structure of coarse and fine grains of both Y_2O_3 and MgO. The fine-grained layers exhibited elongated grains (<100 nm across) resembling to a lamellar eutectic microstructure, while the coarser layers the grains were more equi-axed, measuring up to 400 nm in diameter. Further analysis is required to elucidate the mechanism of formation for this layered structure, but we note that the layers could be consistent with a hypoeutectic solidification microstructure. Since the average magnesia



content (50 vol.%) is much higher than that of the eutectic mixture (13.7 vol.%), the coarse-grained layers could correspond to the formation of equi-axed proeutectic magnesia grains at preferential nucleation sites, and the fine-grained layers could be eutectic formed when the remaining liquid is enriched in yttria ejected from these magnesia grains. Preliminary EDXS data obtained from this microstructure in the TEM (not presented here) appear to support this hypothesis: in the coarse-grained region the grains are almost pure Y_2O_3 and MgO , whereas in the fine-grained region the average composition is close to that of the eutectic.

It is important to reiterate that these deposits were obtained from a multiple scan single line spray, where the plasma gun was programmed to scan across the substrate on a fixed single line. The heat flux from the plasma to the substrate in such a deposition process would be considerably higher than that in a normal raster scan coating deposition. This will greatly reduce the cooling rates of splats and also lead to coarsening of grains in the already deposited materials. The actual microstructural characteristics of the SPPS deposits, without the heat flux effect from the plasma, can only be determined from a single scan spray process where the plasma gun is programmed to scan once across the substrate to deposit only one layer of materials. Data from one such experiment was presented in Fig. 12. The splat contained a mixture of amorphous and crystalline regions, and thus it may be necessary to interpret SPPS microstructures in terms of a combination of solidification and solid-state crystallization processes. It was also noted that the interface between the splats and the substrate contained many unmelted crystalline particles. The presence of such particles at the coating/substrate interface for multipass deposits (such as in practical SPPS coatings) would compromise the integrity of the interface and could reduce significantly the degree of bonding to the substrate.

5. Conclusions

The SPPS process is complex, involving many of the material and processing issues associated with APS and sharing the additional issues of droplet break-up and evaporation of solvents with SPS. It also has several unique issues which include endothermic and exothermic events during chemical changes that are of such a magnitude that they can affect melting, effects of precursor concentration on resulting particle size, and other solution specific effects that can profoundly alter the density of the particles arriving at the substrate. In this work, precursor mixtures used to make Y_2O_3 - MgO ceramic coatings, which tend to have low density, are compared with our most successful precursor for making dense YSZ ceramic coatings. From this comparison, it appears that the two characteristics that distinguish the desirable YSZ precursor from others is the propensity for the YSZ precursor to form dense oxide particles and the absence of endothermic events during pyrolysis. Dense particles

are better at making dense coatings because they will impinge on the substrate at near normal incidence (Stokes number effect) and by not introducing porosity from the arriving particle. It has also been demonstrated that combustible additions to precursor solutions, such as ammonium acetate, can improve the melting of the oxide particles formed by pyrolysis of the injected precursors in the plasma jet. However, if the processes are too highly exothermic then the oxide particles may shatter in the plasma, causing them to travel along the colder periphery of the jet; also, the increased heat resulting from excessive exothermic reactions may overheat the substrate. Simple furnace pyrolysis experiments are recommended as a fast precursor screening method where desirable precursors produce dense particles that can be assessed qualitatively by visual inspection or quantitatively by BET measurements. Improved SPPS coatings will require a thorough evaluation of precursor properties and decomposition products. Calorimetric (DSC) measurements can be used to identify undesirable endothermic behavior. The proposed screening methods should aid in such a development process.

Acknowledgments

The authors thank Dr. Dianying Chen for helpful discussions, Dr. Jack Gromek for assistance with the X-ray experiments, and Dr. Roger Ristau for assistance with the FIB, SEM and TEM experiments. This work was supported by Raytheon Company as part of a DARPA-sponsored ONR project.

References

1. P. Fauchais, A. Vardelle, and B. Dussoubs, Quo Vadis Thermal Spraying?, *J. Therm. Spray Technol.*, 2001, **10**, p 44-66
2. R.A. Miller, Current Status of Thermal Barrier Coatings—An Overview, *Surf. Coat. Technol.*, 1987, **30**, p 1-11
3. S.M. Meier, D.K. Gupta, and K.D. Sheffler, Ceramic Thermal Barrier Coatings for Commercial Gas Turbine Engines, *JOM*, 1991, **43**, p 50-53
4. M. Gell, E.H. Jordan, M. Teicholz, B.M. Cetegen, N.P. Padture, L. Xie, D. Chen, X. Ma, and J. Roth, Thermal Barrier Coatings Made by the Solution Precursor Plasma Spray Process, *J. Therm. Spray Technol.*, 2008, **17**, p 124-135
5. J. Karthikeyan, C.C. Berndt, S. Reddy, J.-Y. Wang, A.H. King, and H. Herman, Nanomaterial Deposits Formed by DC Plasma Spraying of Liquid Feedstocks, *J. Am. Ceram. Soc.*, 1998, **81**, p 121-128
6. P.R. Strutt, B.H. Kear, and R. Boland, US Patent no. 6,025,034, 2000
7. L.L. Shaw, D. Goberman, R. Ren, M. Gell, S. Jiang, Y. Wang et al., The Dependency of Microstructure and Properties of Nanostructured Coatings on Plasma Spray Conditions, *Surf. Coat. Technol.*, 2000, **130**, p 1-8
8. H. Chen, S.W. Lee, C.H. Choi, B.Y. Hur, Y. Zeng, X.B. Zheng, and C.X. Ding, Plasma Sprayed Nanostructured Zirconia Coatings Deposited from Different Powders with Nano-Scale Substructure, *J. Mater. Sci.*, 2004, **39**, p 4701-4703
9. O. Tingaud, A. Grimaud, A. Denoirjean, G. Montavon, V. Rat, J.F. Coudert, P. Fauchais, and T. Chartier, Suspension Plasma-Sprayed Alumina Coating Structures: Operating Parameters Versus Coating Architecture, *J. Therm. Spray Technol.*, 2008, **17**, p 662-670

10. L. Xie, X. Ma, E.H. Jordan, N.P. Padture, D.T. Xiao, and M. Gell, Deposition of Thermal Barrier Coatings Using the Solution Precursor Plasma Spray Process, *J. Mater. Sci.*, 2004, **39**, p 1639-1646
11. N.P. Padture, K.W. Schlichting, T. Bhatia, A. Ozturk, B. Cetegen, E.H. Jordan, M. Gell, S. Jiang, T.D. Xiao, P.R. Strutt, E. Garcia, P. Miranzo, and M.I. Osendi, Towards Durable Thermal Barrier Coatings with Novel Microstructures Deposited by Solution Precursor Plasma Spray, *Acta Mater.*, 2001, **49**, p 2251-2257
12. A.D. Jadhav and N.P. Padture, Mechanical Properties of Solution-Precursor Plasma-Sprayed Thermal Barrier Coatings, *Surf. Coat. Technol.*, 2008, **202**, p 4976-4979
13. A. Ozturk and B.M. Cetegen, Modeling of Plasma Assisted Formation of Precipitates in Zirconium Containing Liquid Precursor Droplets, *Mater. Sci. Eng. A*, 2004, **384**, p 331-351
14. E.H. Jordan, L. Xie, X. Ma, M. Gell, N.P. Padture, B. Cetegen et al., Superior Thermal Barrier Coatings Using Solution Precursor Plasma Spray, *J. Therm. Spray Technol.*, 2004, **13**, p 57-65
15. M. Gell, L. Xie, X. Ma, E.H. Jordan, and N.P. Padture, Highly Durable Thermal Barrier Coatings Made by the Solution Precursor Plasma Spray Process, *Surf. Coat. Technol.*, 2004, **177**, p 97-102
16. M. Gell, L. Xie, E.H. Jordan, and N.P. Padture, Mechanisms of Spallation of Solution Precursor Plasma Spray Thermal Barrier Coatings, *Surf. Coat. Technol.*, 2004, **188**, p 101-106
17. L. Xie, D. Chen, E.H. Jordan, A. Ozturk, F. Wu, X. Ma, B.M. Cetegen, and M. Gell, Formation of Vertical Cracks in Solution-Precursor Plasma-Sprayed Thermal Barrier Coatings, *Surf. Coat. Technol.*, 2006, **201**, p 1058-1064
18. A.D. Jadhav, N.P. Padture, E.H. Jordan, M. Gell, P. Miranzo, and E.R. Fuller, Low-Thermal-Conductivity Plasma-Sprayed Thermal Barrier Coatings with Engineered Microstructures, *Acta Mater.*, 2006, **54**, p 3343-3349
19. A.D. Jadhav, N.P. Padture, F. Wu, E.H. Jordan, and M. Gell, Thick Ceramic Thermal Barrier Coatings with High Durability Deposited Using Solution-Precursor Plasma Spray, *Mater. Sci. Eng. A*, 2005, **405**, p 313-320
20. T.W. Coyle and Y. Wang, Solution Precursor Plasma Spray of Nickel-Yttria Stabilized Zirconia Anodes for Solid Oxide Fuel Cell Application, *J. Therm. Spray Technol.*, 2007, **16**, p 898-904
21. A.L. Vasiliev, N.P. Padture, and X. Ma, Coatings of Metastable Ceramics Deposited by Solution-Precursor Plasma Spray: I. Binary $ZrO_2-Al_2O_3$ System, *Acta Mater.*, 2006, **54**, p 4913-4920
22. A.L. Vasiliev and N.P. Padture, Coatings of Metastable Ceramics Deposited by Solution-Precursor Plasma Spray: II. Ternary $ZrO_2-Y_2O_3-Al_2O_3$ System, *Acta Mater.*, 2006, **54**, p 4921-4928
23. T. Bhatia, A. Ozturk, L. Xie, E.H. Jordan, B.M. Cetegen, M. Gell, X. Ma, and N.P. Padture, Mechanisms of Ceramic Coating Deposition in Solution-Precursor Plasma Spray, *J. Mater. Res.*, 2002, **17**, p 2363-2372
24. C.K. Muoto, E.H. Jordan, M. Gell, and M. Aindow, Effects of Precursor Chemistry on the Structural Characteristics of Sol-Gel/Combustion Synthesized Y_2O_3-MgO Nano-Composites, *J. Am. Ceram. Soc.*, 2011, **94**, p 372-381
25. P. Fauchais, Understanding Plasma Spraying, *J. Phys. D Appl. Phys.*, 2004, **37**, p R86-R108
26. C.K. Muoto, E.H. Jordan, M. Gell, and M. Aindow, Phase Homogeneity in Sol-Gel/Combustion Synthesized $MgO-ZrO_2$ Nano Composites, *J. Am. Ceram. Soc.*, 2010, **93**, p 3102-3109
27. O. Unal, T.E. Mitchell, and A.H. Heuer, Microstructures of Y_2O_3 -Stabilized ZrO_2 Electron Beam-Physical Vapor Deposition Coatings on Ni-Base Superalloys, *J. Am. Ceram. Soc.*, 1994, **77**, p 984-992
28. U. Schulz, H. Oettel, and W. Bunk, Texture of EB-PVD Thermal Barrier Coatings Under Variable Deposition Conditions, *Z. Metallkd.*, 1996, **87**, p 488-492
29. D.D. Hass, A.J. Slifka, and H.N.G. Wadley, Low Thermal Conductivity Vapor Deposited Zirconia Microstructures, *Acta Mater.*, 2001, **49**, p 973-983
30. A. Bacciochini, G. Montavon, J. Ilavsky, A. Denoirjean, and P. Fauchais, Porous Architecture of SPS Thick YSZ Coatings Structured at the Nanometer Scale, *J. Therm. Spray Technol.*, 2010, **19**, p 198-206
31. D. Chen, E.H. Jordan, and M. Gell, Effect of Solution Concentration on Splat Formation and Coating Microstructure Using the Solution Precursor Plasma Spray Process, *Surf. Coat. Technol.*, 2008, **202**, p 2132-2138
32. X. Chen, Evaporation Kinetics and Thermophoresis of Particles, *Encyclopedia of Surface & Colloid Science*, P. Somasendaran, and A. Hubbard, Eds., Taylor & Francis Group, New York, 2006, p 2511
33. W.A. Sirignano, *Fluid Dynamics and Transport of Droplets and Sprays*, Cambridge University Press, Cambridge, 1999
34. M.C. Mayoral, J.M. Andres, M.T. Bona, V. Higuera, and F.J. Belzunce, Yttria Stabilized Zirconia Corrosion Destabilization Followed by Raman Mapping, *Surf. Coat. Technol.*, 2008, **202**, p 5210-5216
35. R. Rampon, O. Marchand, C. Filiatre, and G. Bertrand, Influence of Suspension Characteristic on Coatings Microstructure Obtained by Suspension Plasma Spray, *Surf. Coat. Technol.*, 2008, **202**, p 4337-4342